Journal of Solid State Chemistry 182 (2009) 1733–1741

Contents lists available at ScienceDirect

Journal of Solid State Chemistry

journal homepage: www.elsevier.com/locate/jssc

Porosity control in nanoporous carbide-derived carbon by oxidation in air and carbon dioxide

S. Osswald [a,1], C. Portet [a], Y. Gogotsi [a,*], G. Laudisio [a], J.P. Singer [b,1], J.E. Fischer [b], V.V. Sokolov [c], J.A. Kukushkina [c], A.E. Kravchik [c]

[a] Department of Materials Science and Engineering, A. J. Drexel Nanotechnology Institute, Drexel University, Philadelphia, PA 19104, USA
[b] Department of Materials Science and Engineering, University of Pennsylvania, Philadelphia, PA 19104, USA
[c] Ioffe Physico-Technical Institute, Russian Academy of Sciences, St. Petersburg 194021, Russia

ARTICLE INFO

Article history:
Received 26 January 2009
Received in revised form
7 April 2009
Accepted 11 April 2009
Available online 23 April 2009

Keywords:
Oxidation
Carbide-derived carbon
Carbon dioxide
Activation
Porosity

ABSTRACT

Carbide-derived carbons (CDC) allow a precise control over the pore size through the selection of the carbide precursor and varying of the synthesis conditions. However, their pore volume is limited by the carbide stoichiometry. While activation of carbons derived from various organic precursors has been widely studied, this process may similarly be able to increase the pore volume and specific surface area of CDC. Oxidation of carbide-derived carbon in air and CO_2 at different temperatures and times allows for significant increase in pore volume and specific surface area as well as control over average pore size with subnanometer accuracy. The effect of activation and associated changes in the pore volume and surface area on the hydrogen uptake are also discussed.

© 2009 Elsevier Inc. All rights reserved.

1. Introduction

Carbide-derived carbons (CDC), as a new class of nanoporous carbons, have been attracting much attention in the past decade [1–3]. CDCs show a high efficiency in a large number of applications such as hydrogen and methane storage [4,5], electrode material in Li-ion batteries [6] and supercapacitors [7,8], for protein sorbents [9] and adsorption of toxic chemicals from water/air. CDC is a nanoporous carbon material produced by extracting metal atoms from metal carbide via chlorination [1,10] or hydrothermal treatment [11]. These carbons can be manufactured with a large variety of porosities, depending on synthesis conditions such as the carbide precursor, chlorination temperature, time and annealing procedure. Although large pore volumes can be achieved by using precursors with large metal/carbon ratios, pore growth and structure collapse occur when precursors with low carbon contents are used [12]. Practically, it is also more suitable to use low cost precursors such as TiC or SiC which produce about ~55% of porosity in case of conformal transformation. Since chemically CDC is similar to other porous carbons, methods of activation that are used for other carbon materials may be applied to CDC.

Oxidation of carbon, often referred to as activation, has been investigated for decades and is well known as a powerful route to modify the properties (porosity, microstructure, surface chemistry, electrical conductivity, etc.) of carbon materials [13]. Different methods have been developed including chemical activation using molten NaOH and KOH [14,15] or hot acids (HNO_3, H_2SO_4, H_3PO_4) [16] and physical activation in air, CO_2, or steam [17–23]. The properties of activated carbons strongly depend on the activation process and choice of conditions. Even minor changes in the reaction conditions (e.g., temperature, concentration, and time) for the same reagent can lead to significant differences in pore texture, surface chemistry and microstructure [24,25]. Very little has been reported on activation of CDC, although CDC heating in nitrogen, air, CO_2 and water vapor was described in an early patent as a method of residual chlorine removal [26]. Activation of CDC by infiltration with water and fast heating was also mentioned, but no detailed studies of the activation process parameters on CDC structure and properties have been published.

Activation procedures that maximize pore volume and surface area of different carbon materials lead to a broadening of the pore size distribution (PSD) at the same time, which can limit the control over the porosity. In most cases, the required activation conditions depend on the nature of the initial carbon, its porosity, degree of graphitization and surface chemistry [18].

* Corresponding author. Fax: +1 215 895 1934.
E-mail address: gogotsi@drexel.edu (Y. Gogotsi).
[1] Current address: Department of Materials Science and Engineering, Massachusetts Institute of Technology, Cambridge, MA 02139, USA.

0022-4596/$ - see front matter © 2009 Elsevier Inc. All rights reserved.
doi:10.1016/j.jssc.2009.04.017

Of the potential activation techniques, physical activation is particularly advantageous due to its use of inexpensive gaseous reactants and process simplicity. Physical activation in CO_2, steam or air has been widely studied for different activated carbons [19,25,27]. CO_2 is a relatively mild oxidizer, which leads to a better control over the development of microporosity during activation compared to other reagents such as steam, oxygen or air [20–23]. On the other hand, air activation is a low energy/cost process because of the higher reactivity, requiring a lower activation energy as compared to CO_2 or steam [18,27,28]. However, the process is difficult to control. Our previous work has shown that controlled oxidation in air can be very selective and is able to remove amorphous carbon from carbon nanotubes [29] and nanodiamond [30]. Oxidation is therefore potentially suitable to control and modify the porosity of the most common and low-cost CDCs, such as TiC-CDC [31] or SiC-CDC [10], in order to achieve the desired pore volume or size.

In this paper, we report an investigation of the influence of air and CO_2 activation on structure and properties of TiC-CDC and SiC-CDCs and identify the optimal activation conditions to maximize the micropore volume for hydrogen storage and other applications.

2. Experimental

2.1. Materials

By chlorinating TiC (particle size $\leqslant 2\,\mu m$, density $4.93\,g/cm^3$) at 600 °C in a quartz tube furnace, 600 °C-TiC-CDC was produced [31], while chlorination at 1000 and 1300 °C was done in a graphite furnace, as described previously [32]. The sample names "600 °C-TiC-CDC", "1000 °C-TiC-CDC" and "1300 °C-TiC-CDC" refer to the chlorination temperature during CDC synthesis. When the desired temperature was reached, chlorine gas was passed (15 ml/min) through the quartz tube to extract the Ti metal from the sample following reaction:

$$TiC + 2Cl_2(g) \rightarrow TiCl_4(g) + C(s) \quad (1)$$

After chlorination, the furnace was cooled to room temperature under a constant argon flow. A more detailed description of the CDC synthesis is given elsewhere [31]. The synthesized TiC-CDC samples contain traces of Si (<0.2 at%), W (<0.8 at%), Ti (<0.06 at%) and Fe (<0.07 at%), as determined by EDS. 1100 °C-SiC-CDC was synthesized using a chlorination process similar to the one described above [33]. The SiC powder was provided by Superior Graphite with a particle size $\leq 6\,\mu m$ [Ref. 33].

Activation of 1000 °C-TiC-CDC and 600 °C-TiC-CDC was performed in dry air and CO_2 (Airgas), respectively. Approximately 200 mg of CDC powder was placed in a tube furnace for each activation experiment. The quartz tube was then purged at ambient temperature and pressure for 4 h at a constant gas flow (air or CO_2) of ~200 ml/min. Samples were heated at a rate of 25 °C/min under a constant gas flow of ~50 ml/min until the desired activation temperature was reached. After activation, the furnace was turned off and samples were cooled to room temperature.

2.2. Characterization

Raman analysis was performed using a Renishaw 1000/2000 Raman microspectrometer with a 514 nm Ar^+ laser (1800 l/mm grating, 50× Objective, max. $800\,W/cm^2$) in backscattering geometry.

The pore structure of the TiC-CDCs was characterized by gas sorption measurements using a Quadrasorb apparatus (Quantachrome Instruments) in N_2 at 77 K and CO_2 at 273 K. The specific surface area (BET-SSA) was calculated using Brunauer–Emmett–Teller (BET) analysis from N_2 sorption. The pore size distribution was determined from N_2 and CO_2 isotherms using the non-local density functional theory model (NLDFT), which assumed slit pores [34]. The volume of pores below 1.5 nm (micropores) was calculated from CO_2 sorption, using the same NLDFT model. The porosity of SiC-CDC was measured using Quantachrome Autosorb-1 with Ar adsorbate at −195.8 °C. Sorption isotherms were analyzed by Quantachrome's data reduction software (version 1.27) [34].

Thermogravimetric analysis (TGA) was performed using a SDT 2960 DTA-TGA from TA instruments. Samples were heated from 25 to 800 °C at 2 °C/min under a constant air flow of 40 ml/min.

The H_2 uptake was measured using a Sieverts type apparatus at 77 K and high pressure (60 bar) as described elsewhere [35].

3. Results and discussion

3.1. Raman characterization of as-produced CDC

Fig. 1 shows the Raman spectra of TiC-CDC chlorinated at 600, 1000 and 1300 °C, respectively; 600 °C-TiC-CDC (Fig. 1a) exhibits broad D and G bands of similar intensity at 1351 and 1595 cm^{-1},

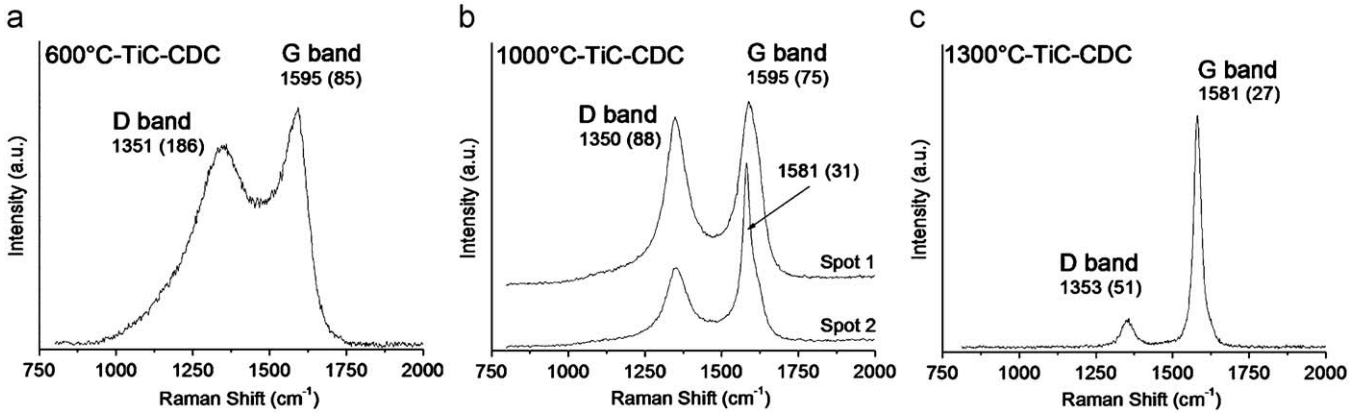

Fig. 1. Raman spectra of TiC-CDC synthesized at chlorination temperatures of 600 °C (a), 1000 °C (b) and 1300 °C (c). With increasing chlorination temperature, D and G bands are sharpened. Full-width at half maximum (FWHM) values are shown in brackets.

with a full-width at half maximum (FWHM) of 186 and 85 cm^{-1}, respectively, indicating the presence of mainly amorphous sp^2 carbon. At low chlorination temperatures, TiC-CDC is constituted mainly of amorphous carbon and little or no graphite, in agreement with earlier studies [31]. While for 1000 °C-TiC-CDC (Fig. 1b) both Raman peaks are noticeably sharpened, shape and intensity distribution somewhat vary for different sample spots. Chlorination at high temperatures leads to increasing graphitization and a less homogeneous sample composition. Raman spectra recorded from regions of high graphitization show a sharp (FWHM ~31 cm^{-1}) and intense G band at ~1581 cm^{-1}. Amorphous parts of the sample exhibit intensity ratios comparable to that of 600 °C-TiC-CDC, while the FWHM of the D band is reduced to about ~88 cm^{-1}, suggesting a general increase in bond ordering. Previous HRTEM studies showed that TiC-CDC becomes more organized at higher chlorination temperatures and carbon atoms reassemble into curved graphene sheets and graphitic ribbons with interplanar spacing close to that of graphite (<0.34 nm) [31]; 1300 °C-TiC-CDC exhibits a higher homogeneity compared to 1000 °C-TiC-CDC. Both D (1353 cm^{-1}) and G band (1581 cm^{-1}) are significantly sharpened, showing FWHM values of 51 and 27 cm^{-1}, respectively. The low D band intensity, a G band position of 1581 cm^{-1} and the reduced peak width of both Raman bands suggest a high level of graphitization.

3.2. Oxidation in air

In order to identify the optimal temperature range for the activation, we performed TGA on the three TiC-CDC samples in air. Fig. 2 shows weight loss and derivative weight fraction ($d\alpha/dT$) during activation as a function of the oxidation temperature. The activation energies (E_A) were calculated using the Achar–Brindley–Sharp–Wendworth method [36–38] and are 138 and 210 kJ/mol for 600 °C-TiC-CDC and 1300 °C-TiC-CDC, respectively, and 120 (E_A^I) and 198 kJ/mol (E_A^{II}) for 1000 °C-TiC-CDC, which showed two different regimes, probably corresponding to oxidation of amorphous (I) and graphitic (II) carbon.

The weight loss between 350 and 550 °C results mainly from the oxidation of amorphous carbon and 600 °C-TiC-CDC (Fig. 2a) and 1000 °C-TiC-CDC (Fig. 2b) show similar oxidation behavior and activation energies. At temperatures above 550 °C, 600 °C-TiC-CDC and 1000 °C-TiC-CDC differ in burn-off rates. The composition of 600 °C-TiC-CDC does not change during oxidation due to the high homogeneity of the sample (Fig. 2a). However, in case of 1000 °C-TiC-CDC, the remaining ~40 wt% mainly consist of graphitized carbon showing a higher resistance to oxidation compared to amorphous material (Fig. 2b). At elevated temperatures (>550 °C) the activation energy of 1000 °C-TiC-CDC (E_A^{II} = 198 kJ/mol) is similar to that of 1300 °C-TiC-CDC (210 kJ/mol), which exhibits a high level of graphitization and therefore requires higher oxidation temperatures (>500 °C).

TGA analysis shows that oxidation of TiC-CDC (in air) does not start below 350 °C, but occurs at a reasonable rate between 400 and 450 °C in case of 600 °C-TiC-CDC and 1000 °C-TiC-CDC. The graphitized 1300 °C-TiC-CDC requires significantly higher oxidation temperatures (>500 °C) and is therefore less favorable for activation. Moreover, the higher synthesis temperature leads to an increase in the average pore size and a broadened pore size distribution. We therefore focused our efforts on activation of 600 °C-TiC-CDC and 1000 °C-TiC-CDC, and set the initial activation temperature to 430 °C in order to achieve sufficient control over the porosity development. Changes in porosity of 1000 °C-TiC-CDC after activation (in air) for 3, 6.5 and 10 h at 430 °C are shown in Fig. 3. The BET-SSA increases with activation time (Fig. 3a) reaching a maximum value of ~1800 m^2/g after 6.5 h with no further increase at higher burn-off. A similar saturation of the BET-SSA has been observed during activation of other carbon materials [39]. Related changes in the pore volume are shown in Fig. 3b. The total pore volume increases from 0.7 to 0.78 (+11.4%), 0.84 (+20%) and 0.87 (+24%) after activation for 3, 6.5 and 10 h, respectively, while the micropore volume, corresponding to the volume of pores smaller than 1.5 nm, increases from 0.34 to 0.36 cm^3/g (+6%), during activation for 3 h, but stabilizes around 0.36 cm^3/g for longer activation times. The observed porosity development may be explained by a two-step process starting with (1) the formation of new micropores at moderate conditions, and (2) widening into larger pores for longer times, leading to an increase of the total pore volume [19,21]. Fig. 3c shows changes in SSA and burn-off during activation for 3 and 6.5 h at different temperatures between 400 and 550 °C. The BET-SSA increases with burn-off (weight loss) at lower activation temperatures, reaches a maximum value of ~1800 m^2/g after 6.5 h at 425 °C and 3 h at 475 °C, respectively, but shows no further increase with burn-off at higher temperatures.

The corresponding changes in pore volume are shown in Fig. 3d. While the total pore volume significantly increases with activation temperature (up to 55%), the micropore volume shows a small increase (+6%) at low temperature, but decreases at higher activation temperatures, suggesting the enlargement of micropores into mesopores.

Our results demonstrate that activation in air at lower temperatures (~430 °C) and for long activation times (>6.5 h) leads to the highest micropore volume (+6%) and

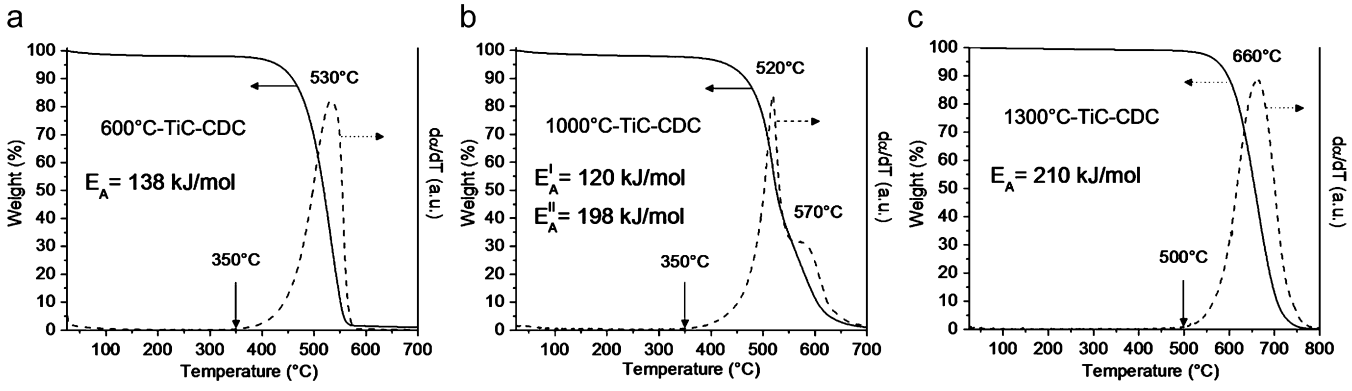

Fig. 2. TGA (solid lines) and derivate weight fraction (dashed lines) of TiC-CDC chlorinated at 600 °C (a), 1000 °C (b) and 1300 °C (c). Experiments conducted in air at 2 °C/min.

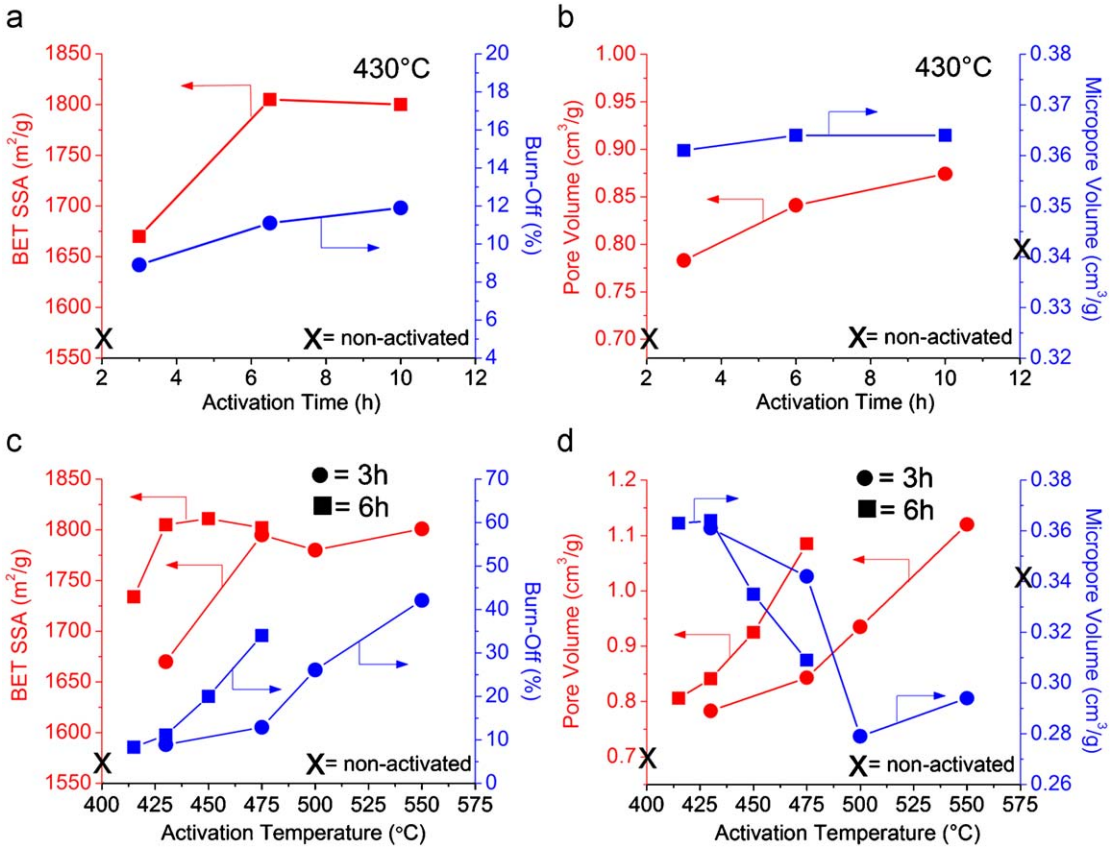

Fig. 3. Changes in SSA (a) and pore volume (b) after activation of 1000 °C-TiC-CDC in air at 430 °C for different times. Similar trends were found for SSA (c) and pore volume (d) after activation for 3 h (circles) and 6 h (squares) between 400 and 550 °C.

BET-SSA (+14%) values at a weight loss of just ~10%, which is much lower than 40%, typical for manufacturing of activated carbons [22,40,41]. The total pore volume increases (up to 60%) with burn-off, and reaches a maximum for high activation temperatures and long activation times. The optimum activation conditions with respect to a high BET-SSA at a low weight loss are 6.5 h at 430 °C and 3 h at 475 °C.

The resulting changes in the pore-size distribution of 1000 °C-TiC-CDC after activation in air are shown in Fig. 4. It should be noted that, jaggedness in the PSDs are a result of the numerical model rather than an actual feature of the pore structure. Oxidation of 1000 °C-TiC-CDC for 3 h at 430 °C (Fig. 4a) leads to a slight increase in the volume of pores smaller than 0.8 nm. Increasing oxidation time reduces the contribution of small pores to the total pore volume, shifting the average pore-size from 1.10 (non-activated) to 1.20 and 1.25 nm after 3 and 6 h activation at 430 °C, respectively. An increase in activation temperature at constant activation time leads to a decrease of the pore volume for pore sizes below 0.8 nm (Fig. 4b) and to formation of larger pores (>2 nm). The average pore size changes from 1.10 (non-activated) to 1.22, 1.50 and 1.90 nm after 6.5 h activation at 415, 450 and 475 °C, respectively.

The results of activation in air demonstrate the possibility of increasing the porosity of TiC-CDC; however, BET-SSA and pore volume showed only a moderate increase and were accompanied by a large weight loss. The micropore volume, which is crucial for many CDC applications [42,43], remained almost unchanged, and mesopores appear at high activation temperatures and long activation times leading to an increase in the total pore volume and BET-SSA saturation.

3.3. Oxidation in CO_2

In an attempt to achieve an increase in the micropore volume, 600 °C-TiC-CDC was activated using CO_2. Graphitization and ribbon formation in high-temperature CDCs such as 1000 °C-TiC-CDC and 1300 °C-TiC-CDC lead to relatively large pore sizes and are therefore unfavorable for most CDC applications. The lower chlorination temperature of 600 °C-TiC-CDC minimizes the formation of graphitic carbon (Fig. 1). Fig. 5 shows changes in BET-SSA and porosity of 600 °C-TiC-CDC after activation at various conditions. At constant activation time (2 h), the BET SSA is proportional to the burn-off and increases with temperature from about 1300 m^2/g (non-activated) to >3000 m^2/g at 950 °C (Fig. 5a). At 875 °C, both total pore volume (+28%) and micropore volume (+18%) increase compared to non-activated 600 °C-TiC-CDC (Fig. 5b). While the total pore volume follows the trend of the BET SSA and increases with increasing activation temperature (+150% at 950 °C), the micropore volume decreases (−8% at 950 °C), falling below that of non-activated 600 °C-TiC-CDC (Fig. 5b). Fig. 5c compares burn-off and BET SSA of 600 °C-TiC-CDC for different activation times at 875 and 950 °C, respectively. BET SSA and burn-off follow similar trends for both activation temperatures and increase with activation time. While at lower activation temperatures, BET-SSA and burn-off after ~8 h

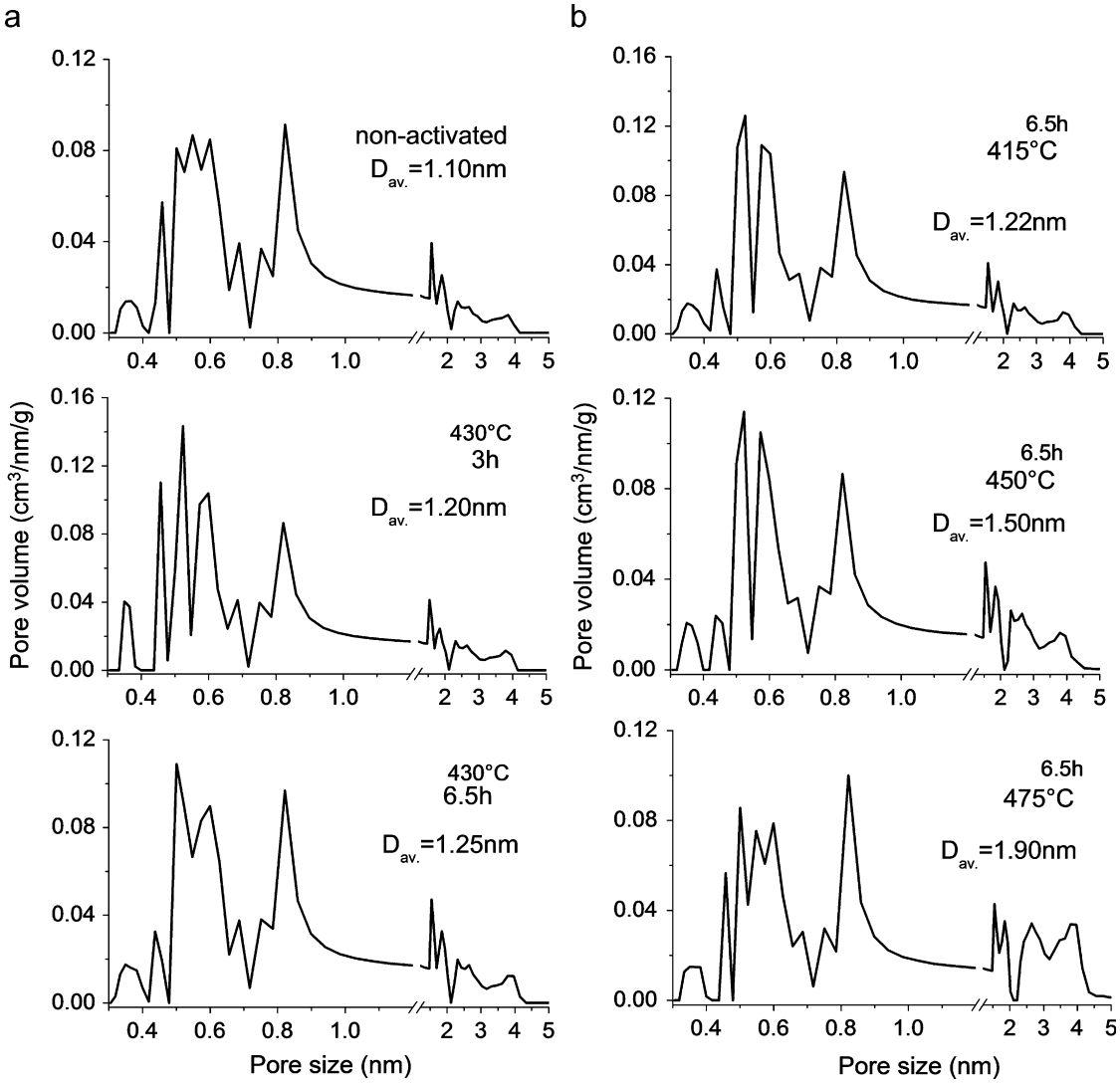

Fig. 4. Pore-size distribution and average pore diameter (D_{av}) of 1000 °C-TiC-CDC after activation in air for 3 and 6.5 h at 430 °C (a) and 6.5 h at 415, 450 and 475 °C (b).

approach a maximum value of ~2700 m^2/g and ~55 wt%, respectively, values up to 3100 m^2/g at a weight loss of 75 wt% are obtained at high activation temperatures (950 °C). The corresponding changes in the pore volume are shown in Fig. 5d. The total pore volume follows the trend of the BET SSA and increases with activation time, reaching maximum values of 1.14 cm^3/g (12 h at 875 °C) and 1.34 cm^3/g (2 h at 950 °C). The micropore volume is the highest for short activation times but decreases with time, similar to air activation, following the two-step process with initial formation of new micropores followed by the enlargement of those micropores into mesopores as described above. While activation at lower temperatures leads to an initial micropore volume increase of about 17%, higher temperatures always lead to a micropore volume lower than in non-activated 600 °C-TiC-CDC. The optimum conditions for activation of 600 °C-TiC-CDC in CO_2 with respect to a high BET-SSA, development of micropores and low weight loss are therefore low activation temperatures (~875 °C) and long activation times (>8 h). High temperatures and longer activation times lead to a larger total pore volume, but are unfavorable for the formation of micropores.

The pore size distributions of CO_2-activated 600 °C-TiC-CDC are plotted in Fig. 6. The average pore size shifts towards higher values with increasing activation time (Fig. 6a) and activation temperature (Fig. 6b). Oxidation for 4 and 12 h at 875 °C leads to an increase in the average pore size from 0.73 to 0.96 and 1.51 nm, respectively (Fig. 6a). The observed shift results mainly from a decrease in the pore volume of pores smaller than 0.8 nm due to the formation of larger pores in the size range of 1–2 nm and above. At constant activation temperature, oxidation in CO_2 enlarges small pores with time, thus decreasing micropore and increasing mesopore volume. Similar trends were found for activation at different temperatures (constant time). Activation for 2 h at 875, 925 and 950 °C increases the average pore size from the initial 0.73 to 0.80, 1.35 and 1.52 nm, respectively.

Fig. 7a compares the Raman spectra of 600 °C-TiC-CDC before and after CO_2-activation at 875 and 950 °C for 8 and 2 h, respectively. In order to accurately measure changes in Raman intensity, spectra were fitted using 4 Lorentzian/Gaussian peaks centered at 1170, 1350, 1510, and 1595 cm^{-1}. The Raman bands at 1350 and 1595 cm^{-1} have been assigned to graphitic sp^2 carbon,

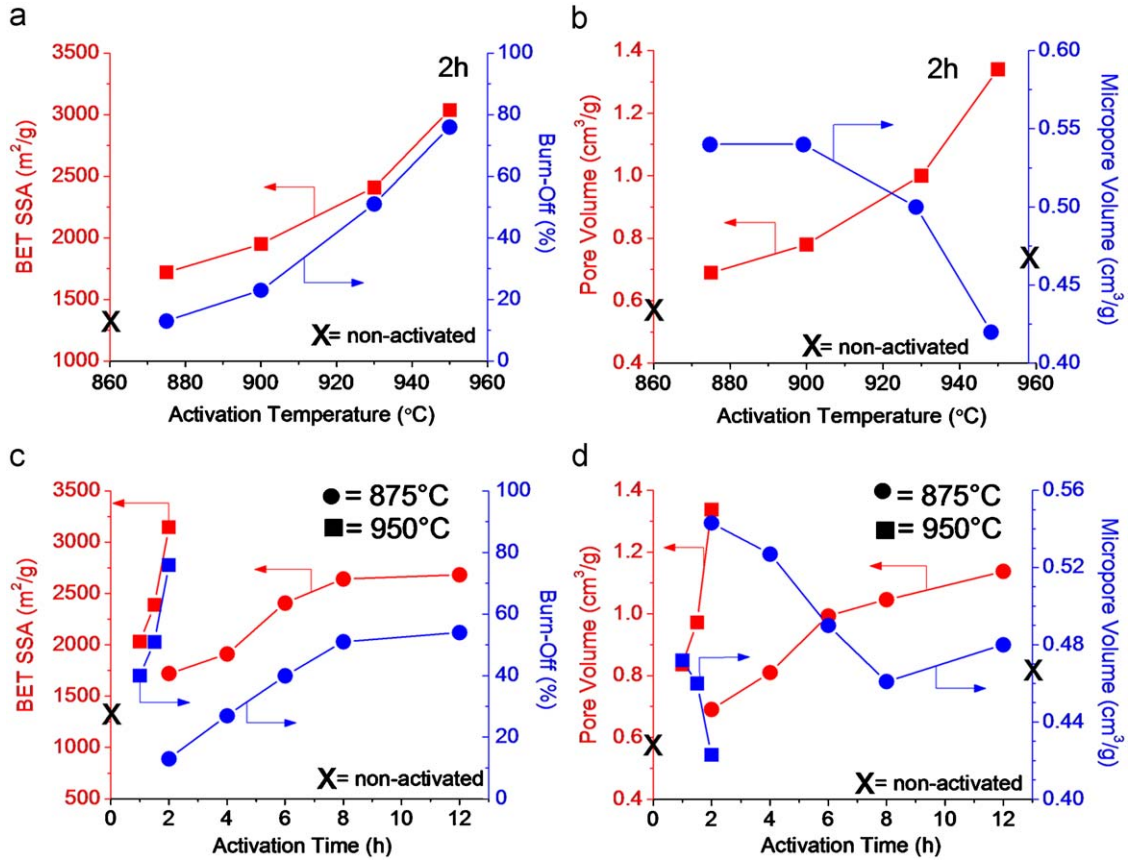

Fig. 5. BET SSA and pore volume of 600 °C-TiC-CDC after oxidation in CO_2 as a function of activation temperature (a, b) and activation time (c, d).

and are referred to as D and G band. Both D and G bands are noticeably sharpened. The FWHM decreases from 186 and 85 cm^{-1} (as-received) to 185 and 83 cm^{-1} (875 °C/8 h) and 178 and 78 cm^{-1} (950 °C/2 h), respectively. The peaks at 1170 and 1510 cm^{-1} are believed to originate from sp^3 carbon phases and C–H contribution or semicircle ring stretch vibrations of benzene, respectively [44]. However, EXAFS [31], EELS [45] and pair distribution function studies [46] show ~10 at% or less of sp^3 carbon in TiC-CDC. The interpretation of changes in the Raman spectrum of CDCs is further complicated by the presence of amorphous carbon and graphite, and functional groups contributing to the Raman signal. Although, the intensity ratio between D and G band has successfully been used to determine the coherence length (crystal size) in graphitic materials such as carbon blacks, great care must be taken with a highly disordered material such as 600 °C-TiC-CDC.

A reduction in the width of the G band (FWHM) and a decrease in the I_D/I_G ratio generally indicate increasing graphitization and/or removal of amorphous carbon [47]. The relative percentage of graphitic carbon increases during activation and the I_D/I_G ratio decreases with activation time (Fig. 7b) and activation temperature (Fig 7c), as expected. A more detailed analysis of the Raman spectra of CDCs is outside the scope of this work.

To confirm that the developed procedure is applicable to other CDCs, we performed several experiments on SiC-CDC [Ref. 48]. The results showed similar trends. BET-SSA, micropore and total pore volume increased by 29%, 67% and 60%, respectively, after CO_2 activation of 1100 °C-SiC-CDC for 1 h at 950 °C. While the oxidation conditions have not been optimized, the results clearly indicate that physical activation under CO_2 is applicable to CDC derived from other metal carbides.

3.4. Hydrogen storage

The ability to control the pore structure of CDCs is of great importance for a large number of applications, especially for adsorption and storage of gases such as hydrogen and methane. Fig. 8 shows the hydrogen excess adsorption isotherms of 1000 °C-TiC-CDC and 600 °C-TiC-CDC measured at high pressure at 77 K after activation in air and CO_2, respectively. The gravimetric H_2 uptake of non-activated 1000 °C-TiC-CDC (2.9 wt%) is lower than that of 600 °C-TiC-CDC (3.3 wt%) due to the higher degree of graphitization and a lower micropore volume [4]. While both air and CO_2 activation of CDC can potentially increase H_2 uptake, the relative increase is larger for CO_2-activated 600 °C-TiC-CDC due to a better porosity development, i.e. 40–50% increase in BET-SSA and micropore volume improvement. The highest H_2 uptake (~4.6 wt%) was measured for 600 °C-TiC-CDC after activation in CO_2 for 2 and 8 h at 950 and 875 °C, respectively. The maximum value is therefore obtained either for CDC having a very high BET-SSA containing larger pores or for CDC with smaller BET-SSA (> 2500 m^2/g) and a high micropore volume. Our results indicate that optimal activation conditions for maximizing H_2 storage capacity is a compromise between high BET-SSA and total pore volume versus the micropore volume; the larger BET-SSA

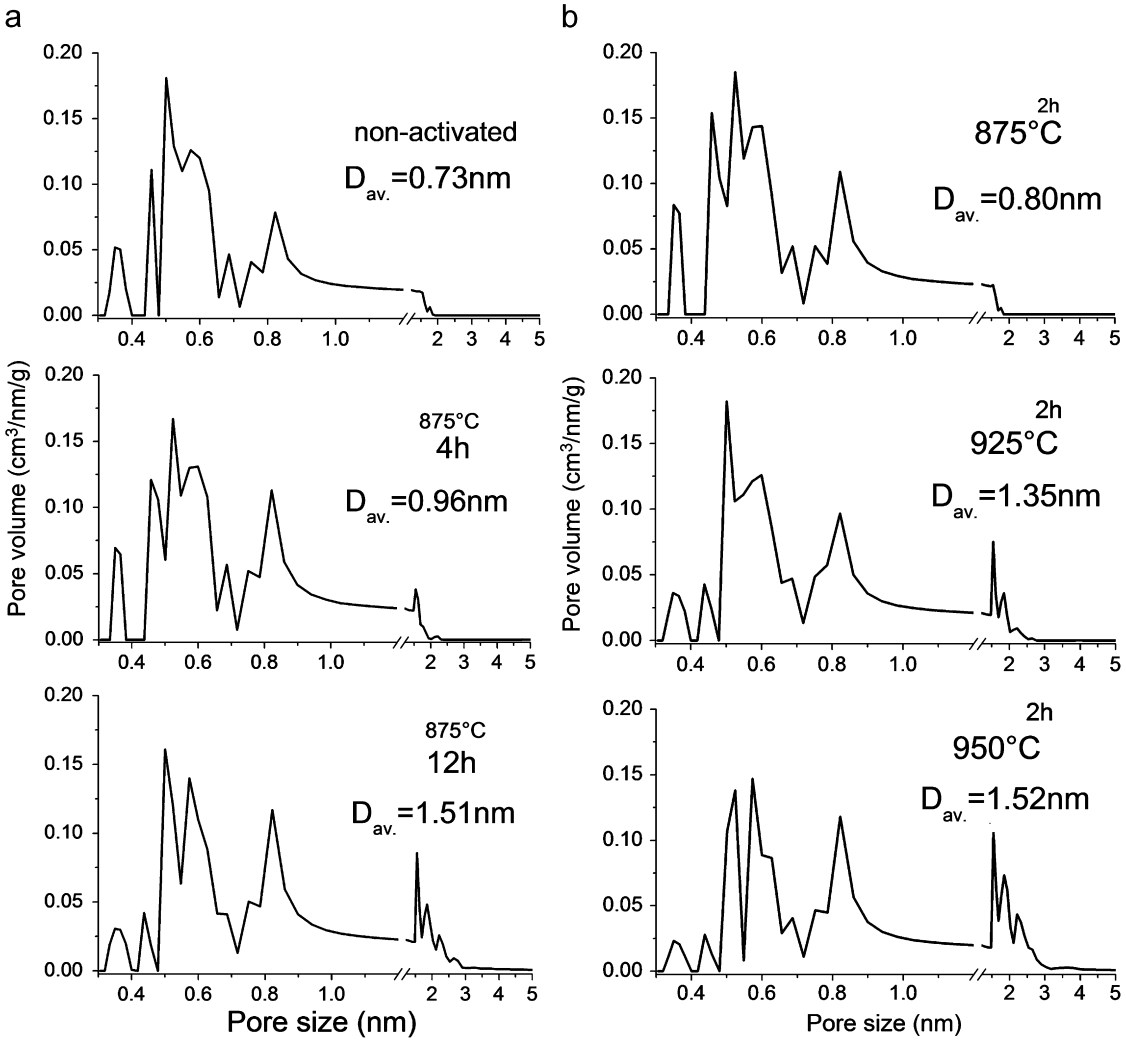

Fig. 6. Changes in pore size distribution and average pore size of 600 °C-TiC-CDC after activation in CO_2 for 4 and 12 h at 875 °C (a) and 2 h at 875, 925 and 950 °C (b).

associated to the volume of bigger pores compensates the decrease in the micropore volume . In the case of 1000 °C-TiC-CDC, best values (3.2 wt%) were obtained after activation in air for 3 h at 475 °C where the micropore volume is maximum as compared to the CDCs activated at higher temperature or for a longer time. This confirms that micropores are more efficient to improve the H_2 storage [4,49]. However, one has to keep in mind that both CDCs differed in structure and porosity before activation. Due to its high homogeneity and a lower graphitization, 600 °C-TiC-CDC is a more adequate candidate for activation. In addition, CO_2 activation allows a better process control and a larger increase in the micropore volume when compared to air activation. The rapid enlargement of the micropores into mesopores during air activation can be attributed to a higher reactivity of O_2, compared to CO_2.

4. Summary and conclusions

We have demonstrated the possibility of adjusting the porosity of CDCs by physical activation in air and CO_2. While air-activation of 1000 °C-TiC-CDC leads to an increase in BET-SSA and total pore volume, the microporosity development remains insufficient to target H_2 storage applications. The high reactivity of O_2 leads to a rapid enlargement of micropores into mesopores and limits the control over porosity development. Activation of 600 °C-TiC-CDC in CO_2, which is a milder oxidizer allowing a better control on the porosity development, leads to a 17% increase in the micropore volume and further improvement in BET-SSA and total pore volume compared to air activation; this results in a 40% increase in gravimetric H_2 uptake to ~4.6 wt%. Furthermore, BET-SSA of above 3000 m^2/g and pore volume of 1.3–1.4 g/cm^3 can be achieved by activation in CO_2. The developed activation method can be applied to other CDCs, such as SiC-CDC, leading to a similar increase in pore volume and BET-SSA.

Our results show that activation in both air and CO_2 can be used to increase the average pore size of CDCs derived from low cost carbides with a high carbon content, such as TiC and SiC. While small pores (<1 nm) are of great importance for hydrogen/methane storage and supercapacitor applications, a larger average pore size (1–5 nm) may be very attractive for sorption of biological molecules and toxins, which are usually larger in size compared to the electrolyte ions or hydrogen molecules.

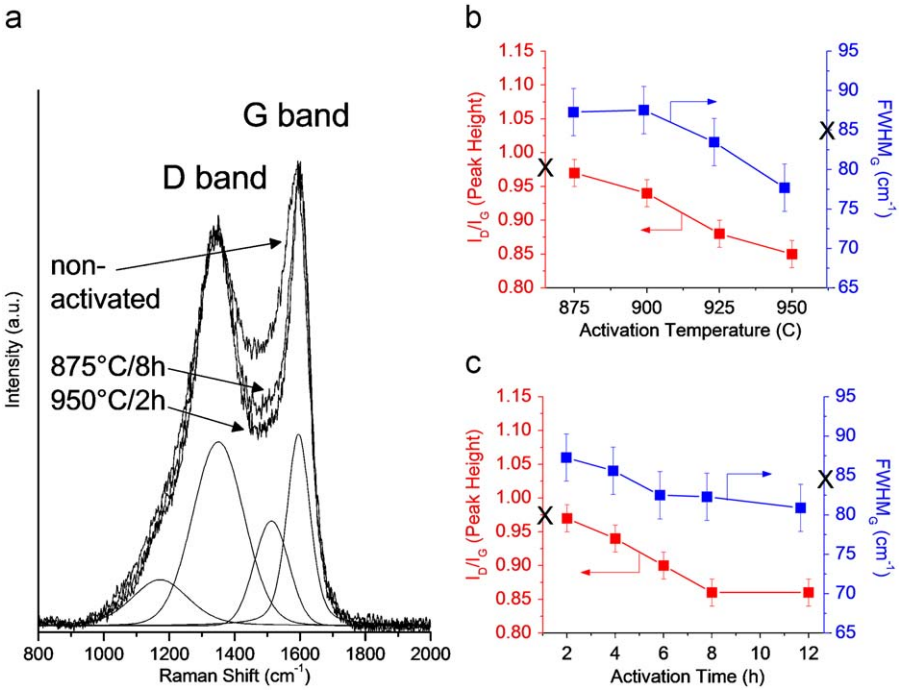

Fig. 7. Changes in the Raman spectrum of 600 °C-TiC-CDC after activation in CO_2 for 2 and 8 h at 950 and 875 °C, respectively (a). I_D/I_G ratio and FWHM decrease with activation temperature at 2 h (b) and activation time at 925 °C (c), suggesting higher ordering and removal of amorphous carbon during activation.

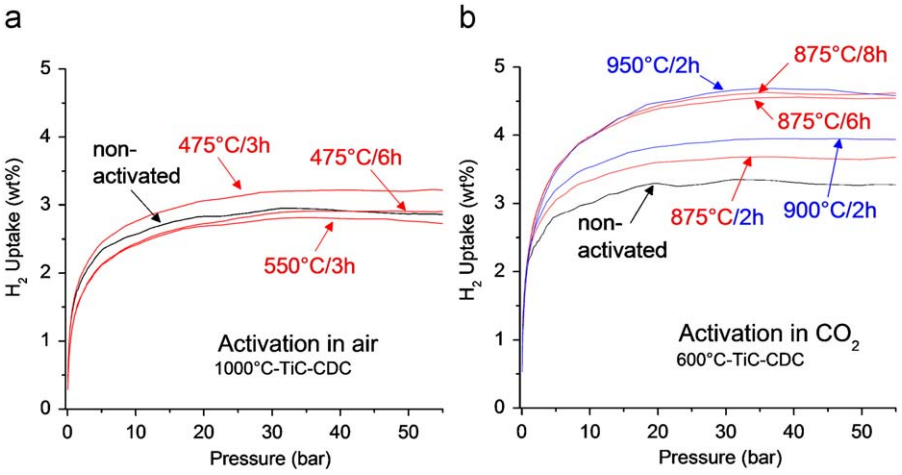

Fig. 8. Hydrogen sorption isotherms (at 77 K) for 1000 °C-TiC-CDC (a) and 600 °C-TiC-CDC (b) after activation in air and CO_2, respectively.

Acknowledgments

We are grateful to Dr. G. Yushin (currently at Georgia Tech) for experimental help and helpful discussions. This work was supported by the US Department of Energy under EERE Grant number DE-FC36-4GO14282.

References

[1] S.K. Gordeev, in: G. Benedek, P. Milani, V.G. Ralchenko (Eds.), NATO ASI on Nanostructured Carbon for Advanced Applications, Kluwer Academic Publishers, Dordrecht, 2001, pp. 71–88.

[2] Y. Gogotsi, A. Nikitin, H. Ye, W. Zhou, J.E. Fischer, B. Yi, H.C. Foley, M.W. Barsoum, Nat. Mater. 2 (2003) 591–594.

[3] G. Yushin, R. Dash, J. Jagiello, J.E. Fischer, Y. Gogotsi, Adv. Funct. Mater. 16 (17) (2006) 2288–2293.

[4] Y. Gogotsi, R.K. Dash, G. Yushin, T. Yildirim, G. Laudisio, J.E. Fischer, J. Am. Chem. Soc. 127 (46) (2005) 16006–16007.

[5] S. Urbonaite, J.M. Juárez-Galán, J. Leis, F. Rodríguez-Reinoso, G. Svensson, Microporous Mesoporous Mater. 113 (1–3) (2008) 14–21.

[6] I.M. Kotina, V.M. Lebedev, A.G. Ilves, G.V. Patsekina, L.M. Tuhkonen, S.K. Gordeev, M.A. Yagovkina, T. Ekstrom, J. Non-Cryst. Solids 299–302 (2) (2002) 820–823.

[7] M. Arulepp, J. Leis, M. Latt, F. Miller, K. Rumma, E. Lust, A.F. Burke, J. Power Sources 162 (2) (2006) 1460–1466.

[8] J. Chmiola, G. Yushin, R. Dash, Y. Gogotsi, J. Power Sources 158 (1) (2006) 765–772.

[9] G. Yushin, E.N. Hoffman, M.W. Barsoum, Y. Gogotsi, C.A. Howell, S.R. Sandeman, G.J. Phillips, A.W. Lloyd, S.V. Mikhalovsky, Biomaterials 27 (34) (2006) 5755–5762.
[10] D. Ersoy, M.J. McNallan, Y.G. Gogotsi, Mater. Res. Innovations 5 (2) (2001) 55–62.
[11] Y.G. Gogotsi, P. Kofstad, K.G. Nickel, M. Yoshimura, Diamond Relat. Mater. 5 (2) (1996) 151–162.
[12] E.N. Hoffman, G. Yushin, T. El-Raghy, Y. Gogotsi, M.W. Barsoum, Microporous Mesoporous Mater. 112 (1–3) (2008) 526–532.
[13] A. Linares-Solano, D. Lozano-Castelló, M.A. Lillo-Ródenas, D. Cazorla-Amorós, Chem. Phys. Carbon 30 (2007).
[14] M.J. Illan-Gomez, A. Garcia-Garcia, C. Salinas-Martinez de Lecea, A. Linares-Solano, Energy Fuels 10 (5) (1996) 1108–1114.
[15] M.A. Lillo-Rodenas, J.P. Marco-Lozar, D. Cazorla-Amoros, A. Linares-Solano, J. Anal. Appl. Pyr. 80 (1) (2007) 166–174.
[16] Y.-R. Nian, H. Teng, J. Electrochem. Soc. 149 (8) (2002) A1008–A1014.
[17] M.J. Munoz-Guillena, M.J. Illan-Gomez, J.M. Martin-Martinez, A. Linares-Solano, C. Salinas-Martinez de Lecea, Energy Fuels 6 (1) (1992) 9–15.
[18] F. Rodriguez-Reinoso, M. Molina-Sabio, Carbon 30 (7) (1992) 1111–1118.
[19] F. Rodríguez-Reinoso, M. Molina-Sabio, M.T. González, Carbon 33 (1) (1995) 15–23.
[20] Z.H. Huang, F.Y. Kang, J.B. Yang, K.M. Liang, R.W. Fu, A.P. Huang, J. Mater. Sci. Lett. 22 (4) (2002) 293–295.
[21] M.V. Navarro, N.A. Seaton, A.M. Mastral, R. Murillo, Carbon 44 (11) (2006) 2281–2288.
[22] J. Pastor-Villegas, C.J. Durán-Valle, Carbon 40 (3) (2002) 397–402.
[23] P.T. Williams, A.R. Reed, Biomass Bioenergy 30 (2) (2006) 144–152.
[24] A. Ahmadpour, D.D. Do, Carbon 34 (4) (1996) 471–479.
[25] J.A. Maciá-Agulló, B.C. Moore, D. Cazorla-Amorós, A. Linares-Solano, Carbon 42 (7) (2004) 1367–1370.
[26] W.A. Mohun, Mineral active carbon and process for producing same, US Patent 3066099, 1962.
[27] G.Q. Lu, D.D. Do, Carbon 30 (1) (1992) 21–29.
[28] E.A. Dawson, G.M.B. Parkes, P.A. Barnes, M.J. Chinn, Carbon 41 (3) (2003) 571–578.
[29] S.Osswald, E. Flahaut, H. Ye, Y. Gogotsi, Chem. Phys. Lett. 402 (4–6) (2005) 422–427.
[30] S. Osswald, G. Yushin, V. Mochalin, S.O. Kucheyev, Y. Gogotsi, J. Am. Chem. Soc. 128 (35) (2006) 11635–11642.
[31] R. Dash, J. Chmiola, G. Yushin, Y. Gogotsi, G. Laudisio, J. Singer, J. Fischer, S. Kucheyev, Carbon 44 (12) (2006) 2489–2497.
[32] A.E. Kravchik, J.A. Kukushkina, V.V. Sokolov, G.F. Tereshchenko, Carbon 44 (15) (2006) 3263–3268.
[33] G. Laudisio, R.K. Dash, J.P. Singer, G. Yushin, Y. Gogotsi, J.E. Fischer, Langmuir 22 (21) (2006) 8945–8950.
[34] P.I. Ravikovitch, A.V. Neimark, Colloids Surf. A: Physicochem. Eng. Aspects 187–188 (2001) 11–21.
[35] W. Zhou, H. Wu, M.R. Hartman, T. Yildirim, J. Phys. Chem. C 111 (44) (2007) 16131–16137.
[36] J.H. Sharp, S.A. Wentworth, Anal. Chem. 41 (14) (1969) 2060–2062.
[37] P.Z. Gao, H.J. Wang, Z.H. Jin, Thermochim. Acta 414 (1) (2004) 59–63.
[38] B.N. Achar, G.W. Brindley, J.H. Sharp, Kinetics and mechanism of dehydroxylation process. III. Applications and limitations of dynamic methods, in: International Clay Conference, Jerusalem, 1966, pp. 67–73.
[39] S. Wei, Z. Li, Z. Yaping, Chin. J. Chem. Eng. 14 (2) (2006) 266–269.
[40] G. San Miguel, G.D. Fowler, C.J. Sollars, Carbon 41 (5) (2003) 1009–1016.
[41] H.M. Mozammel, O. Masahiro, S.C. Bhattacharya, Biomass Bioenergy 22 (5) (2002) 397–400.
[42] C. Largeot, C. Portet, J. Chmiola, P.L. Taberna, Y. Gogotsi, P. Simon, J. Am. Chem. Soc. 130 (9) (2008) 2730.
[43] J. Chmiola, C. Largeot, P.L. Taberna, P. Simon, Y. Gogotsi, Angew. Chem. Int. Ed. 47 (18) (2008) 3392–3395.
[44] J. Schwan, S. Ulrich, V. Batori, H. Ehrhardt, S.R.P. Silva, J. Appl. Phys. 80 (1) (1996) 440–447.
[45] S. Urbonaite, S. Wachtmeister, C. Mirguet, E. Coronel, W.Y. Zou, S. Csillag, G. Svensson, Carbon 45 (10) (2007) 2047–2053.
[46] J.C. Palmer, S.J. Jain, K.E. Gubbins, N. Cohaut, J.E. Fischer, R.K. Dash, Y. Gogotsi, Characterization of porous solids VIII, in: S. Kaskel, P. Llewellyn, F. Rodriguez-Reinoso, N.A. Seaton, (Eds.), Proceedings of the Eighth International Conference on Characterization of Porous Solids, Royal Society of Chemistry, Cambridge, Special Publication No. 318, 2009, pp. 56–63.
[47] A.C. Ferrari, J. Robertson, Philos. Trans. R. Soc. London Ser. A 362 (1824) (2004) 2477–2512.
[48] Z.G. Cambaz, G.N. Yushin, Y. Gogotsi, K.L. Vyshnyakova, L.N. Pereselentseva, J. Am. Ceram. Soc. 89 (2) (2006) 509–514.
[49] M. Jorda-Beneyto, F. Suarez-Garcia, D. Lozano-Castello, D. Cazorla-Amoros, A. Linares-Solano, Carbon 45 (2) (2007) 293–303.